crystals

Article

Two-Dimensional Metal–Organic Framework TM Catalysts for Electrocatalytic N_2 and CO_2 Reduction: A Density Functional Theory Investigation

Anqi She [1], Ming Wang [1], Shuang Li [1], Yanhua Dong [1,*] and Dandan Wang [2,*]

1 Department of Mathematics and Computer Science, Jilin Normal University, Siping 136000, China; a15526580128@jlnu.edu.cn (A.S.); wm@jlnu.edu.cn (M.W.); 0412201-ls@163.com (S.L.)
2 Key Laboratory of Functional Materials Physics and Chemistry of Ministry of Education, College of Physics, Jilin Normal University, Changchun 130103, China
* Correspondence: computerdyp@jlnu.edu.cn (Y.D.); mila880227@126.com (D.W.)

Abstract: In this study, we screened novel two-dimensional metal–organic framework (MOF) materials, which can be used as efficient electrocatalysts in the N_2 reduction reaction (NRR) and CO_2 reduction reaction (CO_2RR) through density functional theory (DFT) calculations. By systematically investigating the adsorption behaviors of N_2 and CO_2 in different MOF-TMs (TM = Fe, Co, Ni, Cu, Zn) and their electrocatalytic hydrogenation processes, we found that 2D MOF-Fe, MOF-Co, and MOF-Ni can be used as catalysts for electrocatalytic NRR. The free energy increase in the corresponding potential-limiting step is calculated to be 0.84 eV on MOF-Fe, 1.00 eV on MOF-Co, and 1.17 eV on MOF-Ni, all of which are less than or at least comparable to those reported values for the NRR. Moreover, only 2D MOF-Fe was identified as a suitable electrocatalyst for CO_2RR. Instead of other hydrocarbons, the product CH_3OH is selectively obtained in an electrocatalytic CO_2 reduction reaction on a 2D MOF-Fe with a free energy increase of 0.84 eV in the potential-limiting step. Overall, the results of this study not only facilitate the potential application of 2D MOF-TMs as electrocatalysts but also provide new guidelines for rationally designing novel electrocatalysts for the NRR and CO_2RR.

Keywords: metal–organic frameworks; DFT calculations; electrocatalyst; nitrogen reduction reactions; carbon dioxide reduction reactions

Citation: She, A.; Wang, M.; Li, S.; Dong, Y.; Wang, D. Two-Dimensional Metal–Organic Framework TM Catalysts for Electrocatalytic N_2 and CO_2 Reduction: A Density Functional Theory Investigation. *Crystals* **2023**, *13*, 1426. https://doi.org/10.3390/cryst13101426

Academic Editor: Ferdinando Costantino

Received: 31 August 2023
Revised: 13 September 2023
Accepted: 13 September 2023
Published: 26 September 2023

1. Introduction

In recent years, in order to alleviate the dual pressure on the environment and energy, nitrogen fixation and carbon dioxide reduction have become the focus of research. Among the various catalytic reduction methods for N_2 and CO_2 molecules, an electrocatalytic reduction reaction is considered as one of the most advantageous technologies [1–5]. For this reason, the development of new effective electrocatalysts for nitrogen reduction reactions (NRR) and carbon dioxide reduction reactions (CO_2RR) is urgently required. Efforts have been made to explore efficient electrocatalysts, and a significant overlap between the catalysts used for NRRs and CO_2RRs has been found. For example, noble metal catalysts, such as Au, [6–8] Pt, [9–11] Rh, [10,12], and Pd [8,10], are efficient NRR and CO_2RR electrocatalysts due to their electronic properties. Moreover, transition metal oxides, such as TiO_2, [13–15] $WO_{3-}x$, [16,17], MnO_2 [18–20], and CuO [21,22], are considered promising electrocatalysts for the NRR and CO_2RR according to their adjustable electronic structures and low cost. However, despite the development of noble metal and metal oxide electrocatalysts, they are limited by several problems, such as the high price of noble metals and the instability of metal oxides at negative potentials. Therefore, there is a broader interest in developing novel NRR and CO_2RR electrocatalysts with a low cost, high efficiency, and high stability.

Metal–organic frameworks (MOFs), which are one-, two-, or three-dimensional skeletons formed by metal atoms and organic bridging ligands through coordination bonds, are attracting increasing attention in electrocatalysis due to their large specific surface area, high stability, low cost, homogeneous active composition, and dense catalytic sites that are easy to tune. For example, Co-MOF, Fe-MOF, and Cu-MOF have been widely used as electrocatalysts for oxygen evolution reactions since Yaghi et al. reported the first MOFs in 1995 [23–26]. In particular, MOFs including Al-MOFs, Cu-MOFs, and Co-MOFs show great promise and have recently attracted extensive attention regarding applications in electrocatalytic NRRs and CO_2RRs [27–30]. However, MOFs with a three-dimensional morphology have several weak points, such as poor electrical conductivity, low metal utilization, and accessible surface area, which limit their electrocatalytic applications. To bypass these problems, two-dimensional (2D) MOFs with metallic property, unsaturated metal sites, and large surface areas have been investigated and show excellent performance in electrocatalysis [31,32]. Until now, the study of 2D MOFs has mainly focused on synthetic methods and their applications in energy storage [33,34]. There are limited reports on 2D MOFs for both electrocatalytic NRRs and CO_2RRs [35–37]. Therefore, it is of great significance to explore the potential applications of 2D MOFs in electrocatalytic NRRs/CO_2RRs and evaluate the corresponding NRR/CO_2RR performance.

Thus far, many metallic 2D MOFs that contain transition metal (TM) ions (Fe, Co, Ni, Mn, Mo) have been successfully synthesized and studied [35,36,38]. Over the last year, we have designed a 2D ultrathin MOF-Co for highly safe and long-life Li-S batteries [34]. The 2D MOF-Co possesses a unique structure, namely, periodically arranged cobalt atoms coordinated with oxygen atoms causing pseudo-octahedra, which are mutually interconnected by the 1,4-benzenedi-carboxylic acid ligands. Interestingly, the Co sites in Co-O_4 moieties are exposed on the surface. It is expected that the exposed coordination, with unsaturated metal sites on the 2D-MOF surface, can serve as active centers to ensure the high electrocatalytic activity for NRRs and CO_2RRs. Generally, metallic 2D MOFs have a high tunability because transition metals are diverse. Inspired by the above concepts, we studied the electrocatalytic performance of several 2D MOF-TMs (TM = Fe, Co, Ni, Cu, Zn) possessing the same structure as that of the 2D MOF-Co we reported earlier, based on density functional theory (DFT) calculations.

In this study, we first investigated the adsorption behaviors of N_2 and CO_2 molecules towards the surfaces of 2D MOFs. By analyzing the adsorption energy, charge transfer, and corresponding bond lengths of the adsorbates, the interaction between adsorbates and 2D MOFs was clarified. The electrocatalytic NRR and CO_2RR pathways for those chemisorbed molecules on the catalyst surfaces were investigated. Our theoretical results indicate that 2D MOF-Fe is an excellent bi-functional electrocatalyst for both NRRs and CO_2RRs. Moreover, 2D MOF-Co and MOF-Ni exhibit high performance only for electrocatalytic NRRs, while the other 2D MOF-TM materials are not appropriate catalysts for electrocatalytic NRRs or CO_2RRs.

2. Calculation Methods

All calculations were performed in the DFT framework using the Vienna ab initio simulation package (VASP) [39,40]. Generalized gradient approximation (GGA) under the projector-augmented plane wave (PAW) method was used [41–43]. The exchange correlation functions were set in the form of Perdew–Burke–Ernzerhof (PBE) [44,45]. In addition, the DFT-D2 correction method of Grimme was applied to describe van der Waals (vdW) forces [46,47]. The previously prepared 2D MOF-Co possesses a defined geometric structure and its unit cell has the chemical formula of $C_{16}H_{10}O_{10}Co_3$, with triclinic symmetry (space group $P\bar{1}$) [34]. To model other 2D MOF-TMs (TM = Fe, Ni, Cu, Zn), the Co atoms in the 2D MOF-Co structure were replaced by TM atoms. In this study, 2D MOF-TM catalysts were constructed with the p(2 × 2) supercell and with a sufficient vacuum region (20 Å) perpendicular to the surface, as shown in Figure 1. To simulate those structures and the corresponding adsorption configurations, the plane wave truncation energy used was 400 eV, and the energy convergence criterion was set to 10^{-4} eV. The convergence threshold of 10^{-2} eV/Å was applied for force. The Monkhorst-Pack of 3 × 2 × 1 K-points were used for the Brillouin-zone integration. We completed a Bader charge analysis to investigate the oxidation state of the mental center. Calculation results indicated that the oxidation state for the tetra- and six-coordinated metal atoms (the tera- and six-coordinated metal atoms were marked as i and ii by dotted blue circles in Figure 1) were different. The oxidation states of atom-i/ii were 1.15/1.31 for Fe, 1.04/1.28 for Co, 1.02/1.23 for Ni, 1.04/1.20 for Cu, and 1.31/1.39 for Zn.

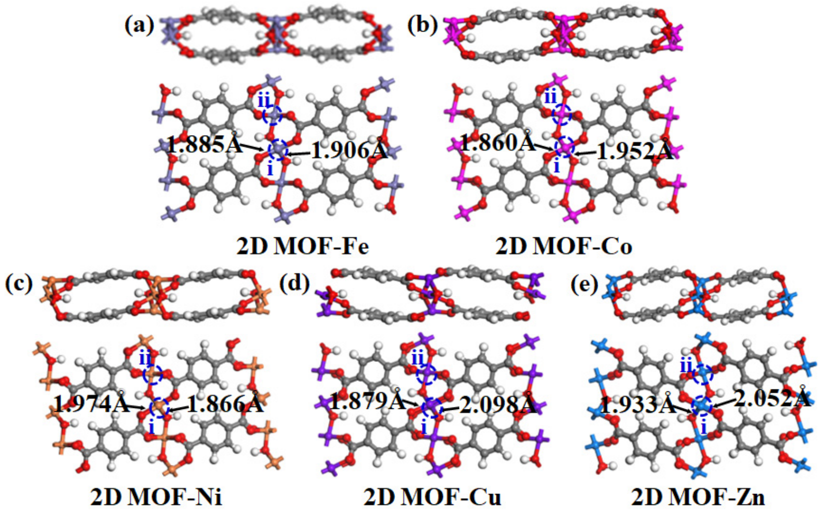

Figure 1. Side and top views of geometric structures for (**a**) MOF-Fe, (**b**) MOF-Co, (**c**) MOF-Ni, (**d**) MOF-Cu, and (**e**) MOF-Zn. Color cards: C: Grey, H: White, O: Red, Fe: Lilac, Co: Pink, Ni: Orange, Cu: Purple, Zn: Sky blue.

To investigate the adsorption of N_2 and CO_2 towards the 2D MOF-TM surface, the isolated N_2 and CO_2 molecules were previously simulated in a large cubic cell of 15 Å in length. The adsorption energies were defined as $E_{ads} = E_{MOF\text{-}gas} - E_{molecule} - E_{MOF}$, where $E_{MOF\text{-}gas}$, $E_{molecule}$, and E_{MOF} are the total energies of the 2D MOF-TM surface with adsorbed N_2 or CO_2 molecules, the isolated N_2 or CO_2 molecule and the clean 2D MOF-TM surface, respectively. A Bader charge analysis and difference charge density calculations were carried out to clarify the interaction between adsorbed molecules and the catalyst surfaces. The electrocatalytic NRR and CO_2RR both involve several coupled proton and electron transfers. To acquire the free energy profiles of electrocatalytic N_2 and CO_2 reduction reactions, the computational electrode model (CHE) was employed [48,49]. According to the CHE, the energy changes are for reactions with the proton–electron pairs ($H^+ + e^-$). The chemical potential of ($H^+ + e^-$) can be obtained through the equation of $\mu(H^+ + e^-) = 1/2\mu(H_2)\text{-}eU$, where $\mu(H_2)$ is the free energy of gaseous H_2 and U is the applied bias. The free energy change (ΔG) at each elementary step of the NRR and CO_2RR processes was calculated using the equation $\Delta G = \Delta E\text{-}neU + \Delta ZPE - T\Delta S$, where ΔE is the change in electron energy calculated by DFT, n is the number of transferred electrons involved in the elementary reaction, ΔZPE is the zero-point energy difference, T is the reaction temperature (in this paper, all are at room temperature, T = 298.15 K), ΔS is the change in entropy value. ΔZPE and ΔS can be obtained through a frequency analysis.

3. Results and Discussion

3.1. Adsorption Behaviors of N_2 and CO_2 on the 2D MOF-TM Surface

In order to evaluate whether MOF-TMs can be used as electrocatalysts for NRR and CO_2RR, the adsorption behaviors of N_2 molecules on the 2D MOF-TM surfaces were systematically investigated firstly. Various molecule adsorption configurations for N_2

towards different sites on the catalyst surfaces were taken into consideration to determine their stable adsorption geometries.

Calculation results show that the adsorption states of N_2 on the MOF-Cu and MOF-Zn surfaces are physically adsorbing, with adsorption energy of −0.11 eV and −0.10 eV, respectively (Figure S1). The physical adsorption modes suggest that the 2D MOF-Cu and MOF-Zn designed in this work are not suitable electrocatalysts for NRRs, while N_2 can be chemisorbed on the other three MOF-TM (TM = Fe, Co, Ni) surfaces at metal sites in end-on configuration (Figure 2a–c). Table 1 summarizes the adsorption parameters for N_2 chemical adsorption (N_2*) towards those three 2D MOF-TM materials. The corresponding adsorption energies of N_2* were calculated to be −1.43 eV, −1.11 eV, and −0.64 eV for MOF-Fe, MOF-Co, and MOF-Ni, respectively. The N-N bond lengths for N_2* on MOF-Fe, MOF-Co, and MOF-Ni, respectively, are 1.139 Å, 1.135 Å, and 1.126 Å, all greater than that of the isolated N_2 molecule (1.117 Å). In addition, newly formed TM-N bonds with bond lengths of 1.773 Å (Fe-N), 1.758 Å (Co-N), and 1.812 Å (Ni-N) were observed. Further difference charge density calculations and Bader charge analyses were carried out to further declare the interaction between N_2* and MOF-Fe/Co/Ni. The difference charge density plots presented in Figure 2 denote that obvious charge redistribution occurs due to the adsorption interaction [49,50]. According to the Bader charge analysis, electrons are transferred from the MOF-TM surface to N_2* and the net obtained charge is 0.27 e, 0.21 e, and 0.09 e for N_2* on MOF-Fe, MOF-Co, and MOF-Ni, respectively. Moreover, the PDOS plots in Figure 3 show that the PDOS peaks for the two N atoms of N_2* are broadly dispersed in comparison with those of the isolated N_2 molecule [51,52]. And, overlap between the N_1 atom and metal atom occurs in the spectrum, especially in the energy ranges of −6.0 eV to −8.0 eV and 2.0 eV to 3.0 eV. According to frequency calculations, the red shifts of the N-N stretching vibrational frequencies for N_2 bound to the Fe, Co, and Ni 2D MOF were 141 cm^{-1}, 103 cm^{-1}, and 23 cm^{-1}, respectively. And, the changes in the N-N stretch frequencies could be used as good indicators for metal-N_2 binding interaction. These above results signify that N_2 molecules can be activated effectively by 2D MOF-Fe/Co/Ni.

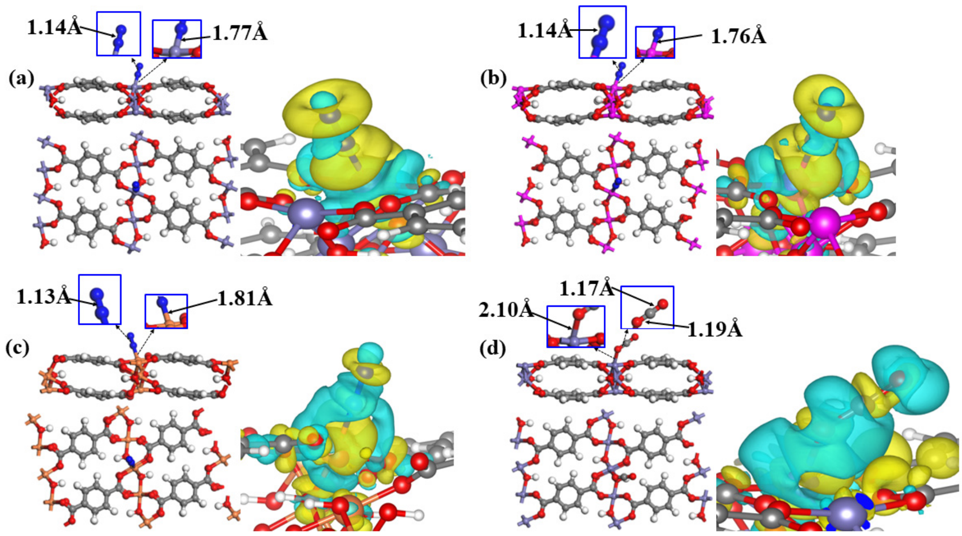

Figure 2. Side and top views of adsorption configurations and the corresponding difference charge density plots for (**a**) N_2 adsorption on MOF-Fe, (**b**) N_2 adsorption on MOF-Co, (**c**) N_2 adsorption on MOF-Ni, (**d**) CO_2 adsorption on MOF-Fe. Color cards: C: Gray, H: White, O: Red, Fe: Lilac, Co: Pink, Ni: Orange, Cu: Purple, Zn: Sky blue. In different charge density plots, the blue (yellow) wireframes denote the loss (gain) of electrons with the isosurface values set as 0.003 $Å^{-3}$.

Table 1. Chemical adsorption parameters for N_2* and CO_2* on 2D MOF-TM surfaces: adsorption energy (E_{ads}), N-N bond length of N_2* (L_{N-N}), C-O bond length of CO_2* (L_{C-O}), the distance between TM sites and N atom of N_2* (d_{TM-N}), the distance between Fe site and the O atom of CO_2* (d_{Fe-O}), the value of net transferred from MOF-TM to N_2* and to CO_2* (Δq), and the redshift values of N-N stretch frequencies with respect to the free N_2 molecule (Δ*k*).

N_2* on MOF-TM	E_{ads} (eV)	L_{N-N} (Å)	d_{TM-N} (Å)	Δq	Δ*k* (cm^{-1})
Fe	−1.43	1.139	1.773	0.27	141
Co	−1.11	1.135	1.758	0.21	103
Ni	−0.64	1.126	1.812	0.09	23
		L_{C-O} (Å)	d_{Fe-O} (Å)		
CO_2* on MOF-Fe	−0.44	1.185/1.172	2.100	0.01	

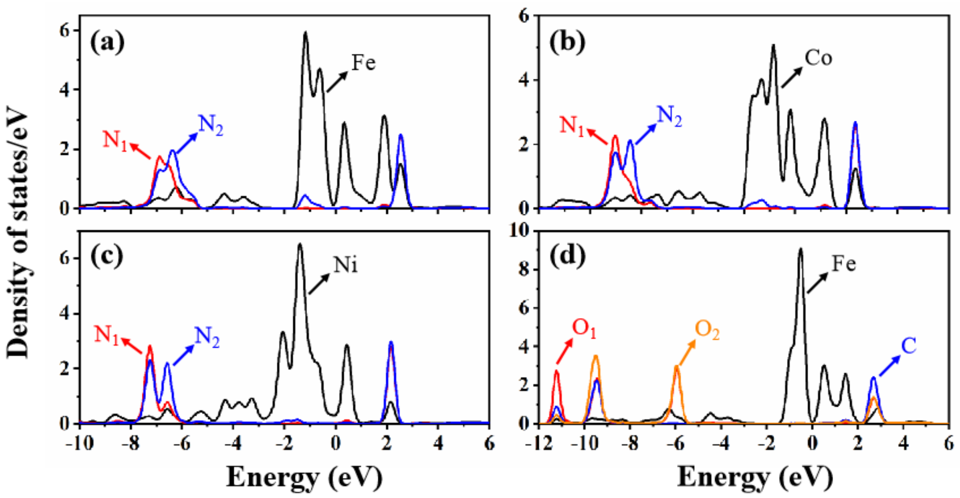

Figure 3. PDOS plots for (**a**) N_2 adsorption on MOF-Fe, (**b**) N_2 adsorption on MOF-Co, (**c**) N_2 adsorption on MOF-Ni, (**d**) CO_2 adsorption on MOF-Fe. The Fermi level was assigned at 0 eV. N_1/O_1 represents the N/O atom bonded with surface metal site, and N_2/O_2 is the N/O atom located far from the metal site.

For CO_2 adsorption on the 2D MOF-TM, various initial adsorption modes were also examined. Full optimization of the initial structures reveals the physical adsorption of CO_2 on MOF-Co, Ni, Cu, and Zn, with a small adsorption energy of −0.21 eV, −0.21 eV, −0.19 eV, and −0.17 eV and with remote distances between the CO_2* and MOF-TM surfaces, as shown in Figure S2. Therefore, those four 2D MOF-TM materials should not be efficient electrocatalysts for CO_2RR. Fortunately, adsorption of CO_2 on the 2D MOF-Fe led to a chemical adsorption state with CO_2* in the linear structure, where electron redistribution between CO_2* and the MOF-Fe surface, and a newly formed bond between the O atom of CO_2* and the Fe site was observed (Figure 2d). The corresponding adsorption parameters for CO_2 on the MOF-Fe were also listed in Table 1. We can see that the adsorption energy was determined to be −0.44 eV and the newly formed O-Fe bond was 2.100 Å. Difference charge density calculations and Bader charge analyses show that the net charge transferred from MOF-Fe to CO_2* was 0.01 e. Similar with N_2*, the PDOS peaks for the C and O atoms of CO_2* are more dispersed compared to those for the isolated CO_2 molecule. And, an obvious overlap between the O_1 atom and the surface Fe atom can be seen in Figure 3d. Significantly, the CO_2 was polarized and activated weakly by the 2D MOF-Fe surface, reflected by the change in C-O bond lengths (1.185 Å and 1.172 Å) in CO_2* relative to those in isolated CO_2 (1.177 Å), and a bent angle of ∠O-C-O = 177.5° for the adsorbed CO_2*.

3.2. Electrocatalytic Processes and Mechanisms for NRR and CO_2RR

Previous reports show that the chemisorption of N_2 and CO_2 on the catalyst surface is favorable for the electrocatalytic N_2 and CO_2 reduction reaction. Therefore, we herein focused on the electrocatalytic NRRs on the 2D MOF-Fe, MOF-Co, and MOF-Ni, and CO_2RRs on the 2D MOF-Fe, according to the above adsorption property calculations.

Figure 4 shows the corresponding free energy changes for each hydrogenation step of the NRR process on the 2D MOF-Fe surface at a zero electrode potential (U = 0 V). The 'solvation corrections' by the COSMO solvation model were obtained with H_2O as the solvent. In the first step of the reaction process, NN* is hydrogenated to NNH* by a coupling reaction with H^+ and e^- pair. In that step, the N-N bond is extended from 1.139 Å to 1.213 Å, and the value of ΔG for this process is 0.84 eV. In the second hydrogenation step, both NNH_2* and NHNH* formations are slightly upslope, with a ΔG of 0.05 eV and 0.03 eV, respectively. The almost identical energy between NNH_2* and NHNH* denotes that alternating and distal pathways happened simultaneously for the first two hydrogenation steps. Subsequently, formations of NH_2NH* and NH_3* are endothermic processes, while $NHNH_2$* formation is exothermic with a ΔG of −0.35 eV and −0.37 eV. Therefore, the third hydrogenation step leads to $NHNH_2$*. Then, NH_2NH_2* rather than NH* + NH_3 is gained by the addition of the fourth H, and the corresponding ΔG value was −0.31 eV. For the subsequent two reaction steps to produce NH_2* + NH_3(g) and NH_3* + NH_3(g), the corresponding ΔG values were −1.24 eV and −0.64 eV, respectively. In the final hydrogenation step, the Fe-N bond length is extended to 1.997 Å, which facilitates the desorption of NH_3 due to the weakened Fe-N bond. Moreover, though the free energy gain for the release of the second NH_3 molecule was calculated to be as large as 1.11 eV, NH_3 release, which can be facilitated by the high solubility of NH_3 in water, is not considered as an elementary reaction of the NRR [52]. According to the above results, the overall NRR process happened along the alternating path and the first hydrogenation step was determined as the potential-limiting step with a free energy increase of 0.84 eV. The free energy increase in the potential-limiting step obtained without solvent corrections is 0.88 eV, almost uniform with the value with solvent corrections, indicating that the solvent effect is weak for NRRs on 2D MOF-metals.

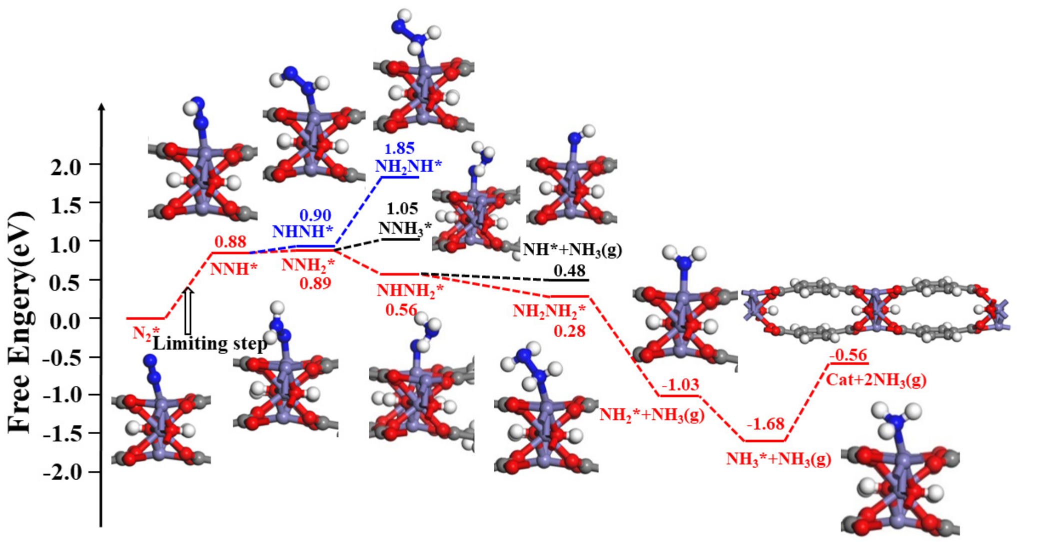

Figure 4. Free energy diagram of the NRR process of N_2* on 2D MOF-Fe and the corresponding geometries of intermediates and products. White, blue, lilac, grey, and red balls denote H, N, Fe, C, and O atoms, respectively.

The structures of the reaction intermediates and the corresponding Gibbs free energy profiles for NRRs on the 2D MOF-Co are shown in Figure 5. The first hydrogenation step results in N-N bonds extended from 1.135 Å to 1.204 Å and the value of ΔG is 1.00 eV. In the second step, NHNH* formation has an advantage over NNH_2* because the energy of

NHNH* was 0.30 eV lower that of NH_2* and NHNH* formation from NNH* is downhill, with a ΔG of −0.25 eV. In the third step, the formation of *$NHNH_2$ is exothermic, at ΔG −0.16 eV. All the subsequent three hydrogenation steps are downhill in free energy, leading to intermediates of NH_2NH_2*, NH_2* + NH_3(g), and NH_3* + NH_3(g), and the corresponding ΔG value is −0.51 eV, −1.04 eV, and −0.95 eV, respectively. The bond length of Co-NH_3* is extended to 1.957 Å and the second NH_3 release needs to overcome the 1.02 eV energy barrier. Overall, the NRR process was along the alternating pathway and the potential-limiting step was determined at the first hydrogenation step, with an energy barrier of 1.00 eV.

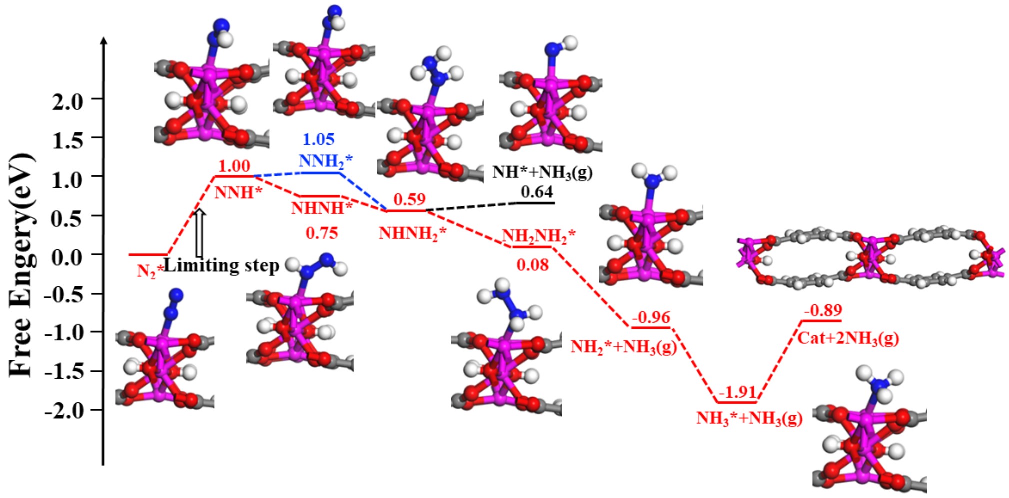

Figure 5. Free energy diagram of the NRR process of N_2* on 2D MOF-Co and the corresponding geometries of intermediates and products. White, blue, pink, grey, and red balls denote H, N, Co, C, and O atoms, respectively.

The electrocatalytic NRR pathways on the 2D MOF-Ni are shown in Figure 6. Similar to the previous two catalytic NRR processes on the 2D MOF-Fe and MOF-Co, the first hydrogenation step is determined as the potential-limiting step and the corresponding energy gain is 1.17 eV. In the same way, the N-N bond is increased from 1.126 Å to 1.201 Å. Note that the first three hydrogenation steps are along the alternating pathway, while the fourth hydrogenation step takes place with a distal mechanism, reflected by the fact that the free energy of $NHNH_3$* was 0.39 eV lower than that of NH_2NH_2*. Then, the fifth and the sixth hydrogenation steps are along the alternating pathway again. Therefore, the NRR process on the 2D MOF-Ni is the mix of alternating and distal pathways. The ΔG values for the second to the sixth hydrogenation step are −0.68 eV, −0.05 eV, −1.26 eV, −0.80 eV, and −1.76 eV, respectively. Moreover, the bond length between the Ni site and the N atom of the second NH_3* is 1.909 Å, much shorter than those between the Fe/Co site and the N atom of NH_3*. Therefore, the desorption energy of the second NH_3 release from the Ni site is 2.43 eV, larger than those values for NH_3 release from the Fe/Co site (1.12/1.02 eV).

The entire electrocatalytic NRR processes of 2D MOF-Fe, MOF-Co, and MOF-Ni were systematically examined. According to the above results, the energy increase in the potential-limiting step for NRRs on the 2D MOF-Fe (0.88 eV), MOF-Co (1.00 eV) and MOF-Ni (1.17 eV) is less than or at least comparable with those reported values of many efficient electrocatalysts for NRRs (0.85 eV on FeN_4 site of FePc [53] 0.85 eV on Nb_3c of SnN_2O_6 nanosheet [54] 1.23 eV on N-C@NiO/GP catalyst [55] 1.47 eV on WO_3-x nanosheet [56]), meaning that the three 2D MOF-TM materials hold immense potential to be used as electrocatalysts for NRRs.

Here we discuss the investigation of electrocatalytic CO_2RRs on the 2D MOF-Fe. The solvent effect is taken into consideration herein. The CO_2 hydrogenation pathway and free energy profiles over the MOF-Fe catalyst are shown in Figure 7. In the hydrogenation process, both the two O sites and C sites of each intermediate were considered for H addition. For the first H addition, OCHO* intermediate instead of OCOH* and OH* + CO* is formed and the free energy gain ΔG was −0.68 eV. The negative value of ΔG signified the easy obtaining of OCHO*. For further hydrogenation, O* + CH_2O and OHCHO* formation, respectively, require ΔG of 1.37 eV and 0.22 eV, while the OCHOH* formation reaction is exothermic with a ΔG of −0.13 eV, indicating that OCHOH* is favorable to form, followed by the hydrogenation of OCHOH* to OCH_2OH* with a free energy uphill and the ΔG was calculated to be 0.16 eV. Then, the fourth H would attack the O site of OCH_2OH*, which is orientated to the surface, resulting in $OHCH_2OH$* with a ΔG of −0.25 eV. The followed CH_3OH formation from the $OHCH_2OH$* hydrogenation is determined as the potential-limiting step with a ΔG of 0.84 eV. Excitingly, CH_3OH is exclusively the carbon products. The ΔG value of 0.84 eV was lower than those values with a range of 0.9~1.1 eV on Cu-based materials, which were known as excellent catalysts for CO_2 electroreduction to hydrocarbons and oxygenates [57,58]. The remaining OH* reacts with the sixth H to form a H_2O* with a ΔG of −0.25 eV. Finally, the H_2O molecule peels off from the catalyst with a desorption energy of −0.20 eV and the surface Fe sites are reactivated. These results indicate that the 2D MOF-Fe is an appropriate electrocatalyst for CO_2RRs with a high efficiency and high product selectivity.

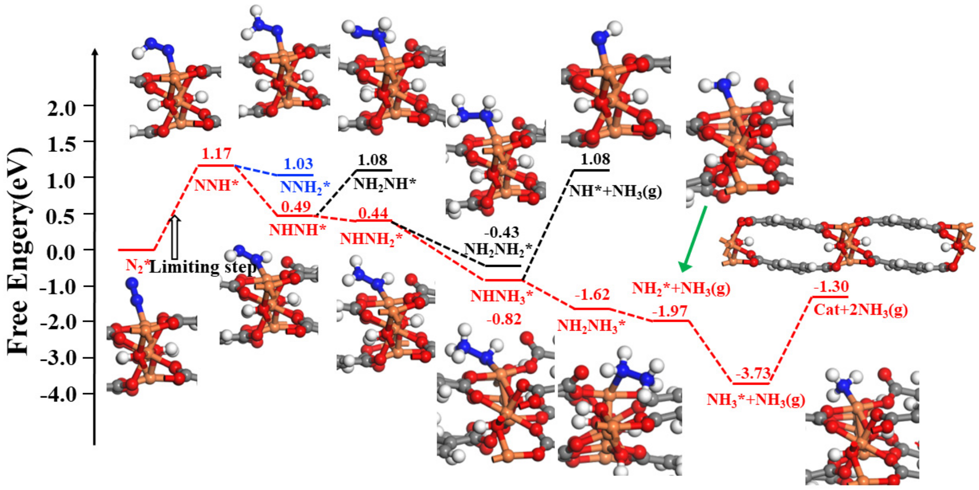

Figure 6. Free energy diagram of the NRR process of N_2* on 2D MOF-Ni and the corresponding geometries of intermediates and products. White, blue, orange, grey, and red balls denote H, N, Ni, C, and O atoms, respectively.

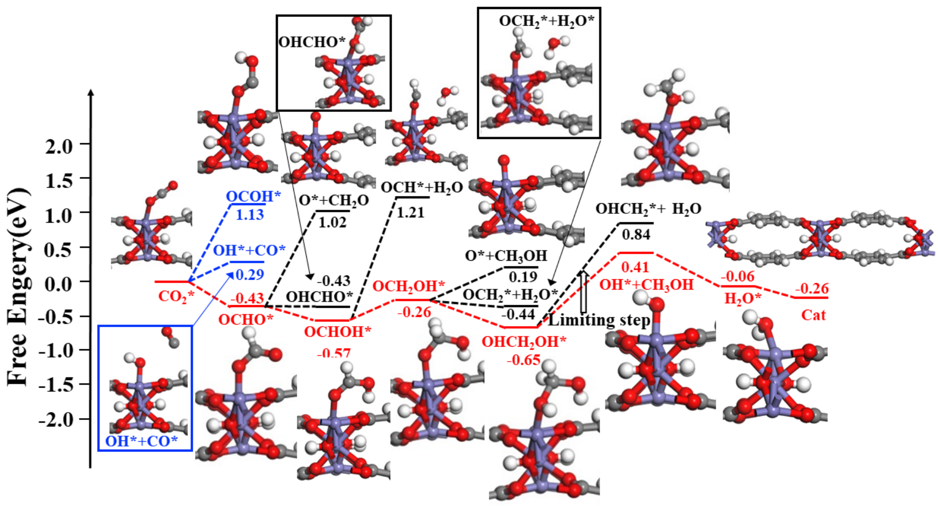

Figure 7. Free energy diagram of the CO_2RR process of CO_2* on 2D MOF-Fe and the corresponding geometries of intermediates and products. White, lilac, grey, and red balls denote H, Fe, C, and O atoms, respectively.

4. Conclusions

In brief, we have systematically investigated the application prospects of five 2D MOF-TMs (TM = Fe, Co, Ni, Cu, Zn) as electrocatalysts for NRRs and CO_2RRs by DFT calculations. The results show that N_2 molecules can be effectively activated by the surface metal site of the 2D MOF-Fe, MOF-Co, and MOF-Ni due to the chemisorption interaction. The appropriate free energy increase in the potential-limiting step (0.84 eV for NRRs on MOF-Fe, 1.00 eV for NRRs on MOF-Co, and 1.17 eV for NRRs on MOF-Ni) signifies that those three 2D MOF-TM materials hold promising applications in NRRs. Furthermore, CO_2 molecules could be selectively reduced to a single hydrocarbon product, CH_3OH, on a 2D MOF-Fe catalyst through the pathway $CO_2^* \rightarrow OCHO^* \rightarrow OCHOH^* \rightarrow OCH_2OH^* \rightarrow OHCH_2OH^* \rightarrow CH_3OH$. And, the fifth hydrogenation step was determined as the potential-limiting step, with a free energy increase of 0.84 eV. These calculation results provide viable approaches to further design and screen the electrocatalysts for NRRs or CO_2RRs.

Supplementary Materials: The following supporting information can be downloaded at: https://www.mdpi.com/article/10.3390/cryst13101426/s1. Figure S1. Side and top views of adsorption configurations for N_2 on (a) MOF-Cu, (b) MOF-Zn. Color cards: C: Grey, H: White, O: Red, Cu: Purple, Zn: Sky blue. Figure S2. Side and top views of adsorption configurations for CO_2 on (a) MOF-Co, (b) MOF-Ni, (c) MOF-Cu, (d) MOF-Zn. Color cards: C: Grey, H: White, O: Red, Co: Pink, Ni: Orange, Cu: Purple, Zn: Sky blue.

Author Contributions: A.S.: Proposed the research idea, Designed the research plan, First draft of the paper. M.W.: Conducted the experiment, Edited the paper. S.L.: Data statistics. Y.D.: Supervision, Project administration, Funding support. D.W.: Study method design, Final version revision, Project administration, Funding support. All authors have read and agreed to the published version of the manuscript.

Funding: This research was funded by National Natural Science Foundation of China (21978110, 51772126, 21801092, and 11904129), the Program for the Development of Science and Technology of Jilin Province (20210101409JC, YDZJ202201ZYTS307, 20200201187JC, 20200801040GH), University-Industry Collaborative Education Program (202002284033). Research on constructing the training system of innovative talents in teachers' major in digital era (JS2360).

Acknowledgments: Computing time granted by the Computing Center of Jilin Province is acknowledged.

Conflicts of Interest: The authors declare no conflict of interest.

References

1. Wang, Q.; Lei, Y.; Wang, D.; Li, Y. Defect engineering in earth-abundant electrocatalysts for CO_2 and N_2 reduction. *Energy Environ. Sci.* **2019**, *12*, 1730–1750. [CrossRef]
2. Xue, X.; Chen, R.; Yan, C.; Zhao, P.; Hu, Y.; Zhang, W.; Yang, S.; Jin, Z. Review on photocatalytic and electrocatalytic artificial nitrogen fixation for ammonia synthesis at mild conditions: Advances, challenges and perspectives. *Nano Res.* **2019**, *12*, 1229–1249. [CrossRef]
3. Zhao, S.; Lu, X.; Wang, L.; Gale, J.; Amal, R. Carbon-Based Metal-Free Catalysts for Electrocatalytic Reduction of Nitrogen for Synthesis of Ammonia at Ambient Conditions. *Adv. Mater.* **2019**, *31*, 1805367. [CrossRef]
4. Zhang, W.; Hu, Y.; Ma, L.; Zhu, G.; Wang, Y.; Xue, X.; Chen, R.; Yang, S.; Jin, Z. Progress and Perspective of Electrocatalytic CO_2 Reduction for Renewable Carbonaceous Fuels and Chemicals. *Adv. Sci.* **2018**, *5*, 1700275. [CrossRef]
5. Wang, G.; Chen, J.; Ding, Y.; Cai, P.; Yi, L.; Li, Y.; Tu, C.; Hou, Y.; Wen, Z.; Dai, L. Electrocatalysis for CO_2 conversion: From fundamentals to value-added products. *Chem. Soc. Rev.* **2021**, *50*, 4993–5061. [CrossRef]
6. Yang, D.-R.; Liu, L.; Zhang, Q.; Shi, Y.; Zhou, Y.; Liu, C.; Wang, F.-B.; Xia, X.-H. Importance of Au nanostructures in CO_2 electrochemical reduction reaction. *Sci. Bull.* **2020**, *65*, 796–802. [CrossRef] [PubMed]
7. Xue, Z.H.; Zhang, S.N.; Lin, Y.X.; Su, H.; Zhai, G.Y.; Han, J.T.; Yu, Q.Y.; Li, X.H.; Antonietti, M.; Chen, J.S. Electrochemical Reduction of N_2 into NH_3 by Donor-Acceptor Couples of Ni and Au Nanoparticles with a 67.8% Faradaic Efficiency. *J. Am. Chem. Soc.* **2019**, *141*, 14976–14980. [CrossRef]
8. Iqbal, M.; Bando, Y.; Sun, Z.; Wu, K.C.; Rowan, A.E.; Na, J.; Guan, B.Y.; Yamauchi, Y. In Search of Excellence: Convex versus Concave Noble Metal Nanostructures for Electrocatalytic Applications. *Adv. Mater.* **2021**, *33*, e2004554. [CrossRef]
9. Chen, D.; Zhu, J.; Pu, Z.; Mu, S. Anion Modulation of Pt-Group Metals and Electrocatalysis Applications. *Chemistry* **2021**, *27*, 12257–12271. [CrossRef]

10. Liu, J.; Ma, Q.; Huang, Z.; Liu, G.; Zhang, H. Recent Progress in Graphene-Based Noble-Metal Nanocomposites for Electrocatalytic Applications. *Adv. Mater.* **2019**, *31*, e1800696. [CrossRef]
11. Chao, T.; Hu, Y.; Hong, X.; Li, Y. Design of Noble Metal Electrocatalysts on an Atomic Level. *ChemElectroChem* **2019**, *6*, 289–303. [CrossRef]
12. Lü, F.; Bao, H.; Mi, Y.; Liu, Y.; Sun, J.; Peng, X.; Qiu, Y.; Zhuo, L.; Liu, X.; Luo, J. Electrochemical CO_2 reduction: From nanoclusters to single atom catalysts. *Sustain. Energy Fuels* **2020**, *4*, 1012–1028. [CrossRef]
13. Liu, J.-Y.; Gong, X.-Q.; Li, R.; Shi, H.; Cronin, S.B.; Alexandrova, A.N. (Photo)Electrocatalytic CO_2 Reduction at the Defective Anatase TiO_2 (101) Surface. *ACS Catal.* **2020**, *10*, 4048–4058. [CrossRef]
14. Wu, T.; Kong, W.; Zhang, Y.; Xing, Z.; Zhao, J.; Wang, T.; Shi, X.; Luo, Y.; Sun, X. Greatly Enhanced Electrocatalytic N_2 Reduction on TiO_2 via V Doping. *Small Methods* **2019**, *3*, 1900356. [CrossRef]
15. Wang, Y.; Jia, K.; Pan, Q.; Xu, Y.; Liu, Q.; Cui, G.; Guo, X.; Sun, X. Boron-Doped TiO_2 for Efficient Electrocatalytic N_2 Fixation to NH_3 at Ambient Conditions. *ACS Sustain. Chem. Eng.* **2018**, *7*, 117–122. [CrossRef]
16. Kong, W.; Zhang, R.; Zhang, X.; Ji, L.; Yu, G.; Wang, T.; Luo, Y.; Shi, X.; Xu, Y.; Sun, X. WO_3 nanosheets rich in oxygen vacancies for enhanced electrocatalytic N_2 reduction to NH_3. *Nanoscale* **2019**, *11*, 19274–19277. [CrossRef] [PubMed]
17. Mendieta-Reyes, N.E.; Díaz-García, A.K.; Gómez, R. Simultaneous Electrocatalytic CO_2 Reduction and Enhanced Electrochromic Effect at WO_3 Nanostructured Electrodes in Acetonitrile. *ACS Catal.* **2018**, *8*, 1903–1912. [CrossRef]
18. Chu, K.; Liu, Y.; Li, Y.-b.; Guo, Y.; Tian, Y.; Zhang, H. Multi-functional Mo-doping in MnO_2 nanoflowers toward efficient and robust electrocatalytic nitrogen fixation. *Appl. Catal. B Environ.* **2020**, *264*, 118525. [CrossRef]
19. Huang, T.; Liu, Z.; Zhang, Y.; Wang, F.; Wen, J.; Wang, C.; Hossain, M.; Xie, Q.; Yao, S.; Wu, Y. Promoting electrocatalytic nitrogen reduction to ammonia via Fe-boosted nitrogen activation on MnO_2 surfaces. *J. Mater. Chem. A* **2020**, *8*, 13679–13684. [CrossRef]
20. Peng, X.; Chen, Y.; Mi, Y.; Zhuo, L.; Qi, G.; Ren, J.; Qiu, Y.; Liu, X.; Luo, J. Efficient Electroreduction CO_2 to CO over MnO_2 Nanosheets. *Inorg. Chem.* **2019**, *58*, 8910–8914. [CrossRef]
21. Yan, X.; Chen, C.; Wu, Y.; Liu, S.; Chen, Y.; Feng, R.; Zhang, J.; Han, B. Efficient electroreduction of CO_2 to C_{2+} products on CeO_2 modified CuO. *Chem. Sci.* **2021**, *12*, 6638–6645. [CrossRef] [PubMed]
22. Fu, W.; Cao, Y.; Feng, Q.; Smith, W.R.; Dong, P.; Ye, M.; Shen, J. Pd-Co nanoalloys nested on CuO nanosheets for efficient electrocatalytic N_2 reduction and room-temperature Suzuki-Miyaura coupling reaction. *Nanoscale* **2019**, *11*, 1379–1385. [CrossRef] [PubMed]
23. Yaghi, O.M.; Li, G.; Li, H. Selective binding and removal of guests in a microporous metal-organic framework. *Nature* **1995**, *378*, 703–706. [CrossRef]
24. Zhang, X.; Sun, W.; Du, H.; Kong, R.-M.; Qu, F. A Co-MOF nanosheet array as a high-performance electrocatalyst for the oxygen evolution reaction in alkaline electrolytes. *Inorg. Chem. Front.* **2018**, *5*, 344–347. [CrossRef]
25. Jiang, S.; Li, S.; Xu, Y.; Liu, Z.; Weng, S.; Lin, M.; Xu, Y.; Jiao, Y.; Chen, J. An iron based organic framework coated with nickel hydroxide for energy storage, conversion and detection. *J. Colloid. Interface Sci.* **2021**, *600*, 150–160. [CrossRef]
26. Jahan, M.; Liu, Z.; Loh, K.P. A Graphene Oxide and Copper-Centered Metal Organic Framework Composite as a Tri-Functional Catalyst for HER, OER, and ORR. *Adv. Funct. Mater.* **2013**, *23*, 5363–5372. [CrossRef]
27. Fu, Y.; Li, K.; Batmunkh, M.; Yu, H.; Donne, S.; Jia, B.; Ma, T. Unsaturated p-Metal-Based Metal-Organic Frameworks for Selective Nitrogen Reduction under Ambient Conditions. *ACS Appl. Mater. Interfaces* **2020**, *12*, 44830–44839. [CrossRef]
28. Pan, Y.; Abazari, R.; Wu, Y.; Gao, J.; Zhang, Q. Advances in metal–organic frameworks and their derivatives for diverse electrocatalytic applications. *Electrochem. Commun.* **2021**, *126*, 107024. [CrossRef]
29. Nam, D.H.; Bushuyev, O.S.; Li, J.; De Luna, P.; Seifitokaldani, A.; Dinh, C.T.; Garcia de Arquer, F.P.; Wang, Y.; Liang, Z.; Proppe, A.H.; et al. Metal-Organic Frameworks Mediate Cu Coordination for Selective CO_2 Electroreduction. *J. Am. Chem. Soc.* **2018**, *140*, 11378–11386. [CrossRef]
30. Khalil, I.E.; Xue, C.; Liu, W.; Li, X.; Shen, Y.; Li, S.; Zhang, W.; Huo, F. The Role of Defects in Metal–Organic Frameworks for Nitrogen Reduction Reaction: When Defects Switch to Features. *Adv. Funct. Mater.* **2021**, *31*, 2010052. [CrossRef]
31. Zhao, K.; Zhu, W.; Liu, S.; Wei, X.; Ye, G.; Su, Y.; He, Z. Two-dimensional metal–organic frameworks and their derivatives for electrochemical energy storage and electrocatalysis. *Nanoscale Adv.* **2020**, *2*, 536–562. [CrossRef] [PubMed]
32. Wen, J.; Li, Y.; Gao, J. Two-dimensional Metal-organic Frameworks and Derivatives for Electrocatalysis. *Chem. Res. Chin. Univ.* **2020**, *36*, 662–679. [CrossRef]
33. Li, F.L.; Wang, P.; Huang, X.; Young, D.J.; Wang, H.F.; Braunstein, P.; Lang, J.P. Large-Scale, Bottom-Up Synthesis of Binary Metal-Organic Framework Nanosheets for Efficient Water Oxidation. *Angew. Chem. Int. Ed. Engl.* **2019**, *58*, 7051–7056. [CrossRef] [PubMed]
34. Li, Y.; Lin, S.; Wang, D.; Gao, T.; Song, J.; Zhou, P.; Xu, Z.; Yang, Z.; Xiao, N.; Guo, S. Single Atom Array Mimic on Ultrathin MOF Nanosheets Boosts the Safety and Life of Lithium-Sulfur Batteries. *Adv. Mater.* **2020**, *32*, e1906722. [CrossRef]
35. Cui, Q.; Qin, G.; Wang, W.; Geethalakshmi, K.R.; Du, A.; Sun, Q. Mo-based 2D MOF as a highly efficient electrocatalyst for reduction of N_2 to NH_3: A density functional theory study. *J. Mater. Chem. A* **2019**, *7*, 14510–14518. [CrossRef]
36. Li, W.; Fang, W.; Wu, C.; Dinh, K.N.; Ren, H.; Zhao, L.; Liu, C.; Yan, Q. Bimetal–MOF nanosheets as efficient bifunctional electrocatalysts for oxygen evolution and nitrogen reduction reaction. *J. Mater. Chem. A* **2020**, *8*, 3658–3666. [CrossRef]
37. Zhou, Y.; Zheng, L.; Yang, D.; Yang, H.; Lu, Q.; Zhang, Q.; Gu, L.; Wang, X. Enhancing CO_2 Electrocatalysis on 2D Porphyrin-Based Metal–Organic Framework Nanosheets Coupled with Visible-Light. *Small Methods* **2020**, *5*, 2000991. [CrossRef]

38. Yuan, M.; Wang, R.; Fu, W.; Lin, L.; Sun, Z.; Long, X.; Zhang, S.; Nan, C.; Sun, G.; Li, H.; et al. Ultrathin Two-Dimensional Metal-Organic Framework Nanosheets with the Inherent Open Active Sites as Electrocatalysts in Aprotic Li-O_2 Batteries. *ACS Appl. Mater. Interfaces* **2019**, *11*, 11403–11413. [CrossRef]
39. Jones, R.O. Density functional theory: Its origins, rise to prominence, and future. *Rev. Mod. Phys.* **2015**, *87*, 897–923. [CrossRef]
40. Wei, Y.; Xing, G.; Liu, K.; Li, G.; Dang, P.; Liang, S.; Liu, M.; Cheng, Z.; Jin, D.; Lin, J. New strategy for designing orangish-red-emitting phosphor via oxygen-vacancy-induced electronic localization. *Light. Sci. Appl.* **2019**, *8*, 15. [CrossRef]
41. Vitos, L.; Kollar, J.; Skriver, H.L. Local density approximation versus generalized gradient approximation: Full charge density study of the atomic volume of the light actinides. *J. Alloys Compd.* **1998**, *271*, 339–341. [CrossRef]
42. Perdew, J.P.; Burke, K.; Ernzerhof, M. Generalized gradient approximation made simple. *Phys. Rev. Lett.* **1996**, *77*, 3865–3868. [CrossRef] [PubMed]
43. Blochl, P.E. Projector augmented-wave method. *Phys. Rev. B Condens. Matter* **1994**, *50*, 17953–17979. [CrossRef] [PubMed]
44. Burke, K.; Perdew, J.P.; Levy, M. Improving energies by using exact electron densities. *Phys. Rev. A* **1996**, *53*, R2915–R2917. [CrossRef] [PubMed]
45. Xu, X.; Goddard, W.A. The extended Perdew-Burke-Ernzerhof functional with improved accuracy for thermodynamic and electronic properties of molecular systems. *J. Chem. Phys.* **2004**, *121*, 4068–4082. [CrossRef] [PubMed]
46. Grimme, S. Semiempirical GGA-type density functional constructed with a long-range dispersion correction. *J. Comput. Chem.* **2006**, *27*, 1787–1799. [CrossRef]
47. Wu, X.; Vargas, M.C.; Nayak, S.; Lotrich, V.; Scoles, G. Towards extending the applicability of density functional theory to weakly bound systems. *J. Chem. Phys.* **2001**, *115*, 8748–8757. [CrossRef]
48. Li, Y.; Su, H.; Chan, S.H.; Sun, Q. CO_2 Electroreduction Performance of Transition Metal Dimers Supported on Graphene: A Theoretical Study. *ACS Catal.* **2015**, *5*, 6658–6664. [CrossRef]
49. Xu, H.; Guan, D.; Ma, L. The bio-inspired heterogeneous single-cluster catalyst Ni100-Fe_4S_4 for enhanced electrochemical CO_2 reduction to CH_4. *Nanoscale* **2023**, *15*, 2756–2766. [CrossRef]
50. Xiao, W.; Kiran, G.K.; Yoo, K.; Kim, J.H.; Xu, H. The Dual-Site Adsorption and High Redox Activity Enabled by Hybrid Organic-Inorganic Vanadyl Ethylene Glycolate for High-Rate and Long-Durability Lithium-Sulfur Batteries. *Small* **2023**, *19*, e2206750. [CrossRef]
51. Guan, D.; Xu, H.; Zhang, Q.; Huang, Y.C.; Shi, C.; Chang, Y.C.; Xu, X.; Tang, J.; Gu, Y.; Pao, C.W.; et al. Identifying A Universal Activity Descriptor and a Unifying Mechanism Concept on Perovskite Oxides for Green Hydrogen Production. *Adv. Mater.* **2023**, *2023*, e2305074. [CrossRef]
52. Yang, H.; Luo, D.; Gao, R.; Wang, D.; Li, H.; Zhao, Z.; Feng, M.; Chen, Z. Reduction of N_2 to NH_3 by TiO_2-supported Ni cluster catalysts: A DFT study. *Phys. Chem. Chem. Phys.* **2021**, *23*, 16707–16717. [CrossRef] [PubMed]
53. He, C.; Wu, Z.-Y.; Zhao, L.; Ming, M.; Zhang, Y.; Yi, Y.; Hu, J.-S. Identification of FeN_4 as an Efficient Active Site for Electrochemical N_2 Reduction. *ACS Catal.* **2019**, *9*, 7311–7317. [CrossRef]
54. Li, X.; Tian, Y.; Wang, X.; Guo, Y.; Chu, K. $SnNb_2O_6$ nanosheets for the electrocatalytic NRR: Dual-active-center mechanism of Nb_{3C} and Sn_{4C}–Nb_{5C} dimer. *Sustain. Energy Fuels* **2021**, *5*, 4277–4283. [CrossRef]
55. Chen, Y.; Wu, B.; Sun, B.; Wang, N.; Hu, W.; Komarneni, S. N-Doped Porous Carbon Self-Generated on Nickel Oxide Nanosheets for Electrocatalytic N_2 Fixation with a Faradaic Efficiency beyond 30%. *ACS Sustain. Chem. Eng.* **2019**, *7*, 18874–18883. [CrossRef]
56. Luo, L.; Wang, B.; Wang, J.; Niu, X. Vacancy engineering of $WO_{3\text{-}X}$ nanosheets for electrocatalytic NRR process—A first-principles study. *Phys. Chem. Chem. Phys.* **2021**, *23*, 16658–16663. [CrossRef]
57. Ren, D.; Fong, J.; Yeo, B.S. The effects of currents and potentials on the selectivities of copper toward carbon dioxide electroreduction. *Nat. Commun.* **2018**, *9*, 925. [CrossRef]
58. Kuhl, K.P.; Cave, E.R.; Abram, D.N.; Jaramillo, T.F. New insights into the electrochemical reduction of carbon dioxide on metallic copper surfaces. *Energy Environ. Sci.* **2012**, *5*, 7050–7059. [CrossRef]